Journal of Energy Chemistry 107 (2025) 872–880

Contents lists available at ScienceDirect

Journal of Energy Chemistry

journal homepage: www.elsevier.com/locate/jechem

http://www.journals.elsevier.com/journal-of-energy-chemistry/

Constructing Ru-P/O-transition metal bridge enabling high-performance oxygen evolution reaction

Fengying Pan [a,1], Cheng Gong [a,1], Yiwen Sun [a], Zeliang Wu [c], Dongfang Li [b], Jiaxin Wu [a], Xianjun Cao [a], Yi Xu [a], Xiaowei Li [a,d,*], Hong Gao [a], Jinqiang Zhang [b,*], Yufei Zhao [b,*], Hao Liu [b,*]

[a] Joint International Laboratory on Environmental and Energy Frontier Materials, School of Environmental and Chemical Engineering, Shanghai University, Shanghai 200444, China
[b] Centre for Clean Energy Technology, Faculty of Science, University of Technology Sydney, Broadway, Sydney, NSW 2007, Australia
[c] School of Resources and Environment, Nanchang University, Nanchang 330031, Jiangxi, China
[d] School of Environmental and Chemical Engineering, Organic Compound Pollution Control Engineering, Ministry of Education, Shanghai University, Shanghai 200444, China

ARTICLE INFO

Article history:
Received 24 April 2025
Revised 12 May 2025
Accepted 14 May 2025
Available online 22 May 2025

Keywords:
Ru cluster
Transition metal phosphides
Oxygen evolution reaction
Mechanism alteration

ABSTRACT

Incorporating low-concentration precious metals into transition metal phosphides (TMPs) may represent a promising strategy to achieve improved catalytic performance of oxygen evolution reaction (OER). We design RuP_4 clusters immobilized on porous NiFeP nanosheets with Ru-P/O-TM bridge (RuP-NiFeP) for effective OER. The Ru-P/O-Ni/Fe bridges formed between the RuP_4 clusters and the NiFeP facilitate electron transfer between oxyphilic Ru atoms and Ni/Fe atoms, enabling Ru to achieve optimized reactant/intermediate adsorption. Advanced characterizations and theoretical calculations reveal that the incorporation of Ru species leads to the upshift of *d* band center and the formation of more disordered γ-NiOOH. The Ru-based clusters and the achieved disordered γ-NiOOH may deliver synergistic effect to further enhance the OER capability of RuP-NiFeP. Moreover, the presence of Ru species shifts the OER mechanism from the absorbate evolution mechanism (AEM) pathway (NiFeP) to the lattice oxygen mechanism (LOM) pathway, with *OH deprotonation (*OH → *O) as the rate-determining step (RDS). The RuP-NiFeP catalyst exhibits remarkable alkaline OER activity, requiring only an overpotential of 225 mV to achieve a current density of 100 mA cm^{-2}, and retains its performance with a minimal current density decay of 1.9% after stability test. This work offers valuable insights into the design of cost-effective and highly efficient electrocatalysts for alkaline OER.

1. Introduction

Oxygen evolution reaction (OER) is deemed a crucial bottleneck for various sustainable energy conversion and storage systems due to their complex and sluggish four-electron transport process, including water splitting system and rechargeable metal-air batteries [1–4]. Noble metal-based materials known as the state-of-the-art OER electrocatalysts, such as ruthenium and iridium-based catalysts, efficiently facilitate the OER process by minimizing the activation free energy and reducing the overpotential [5–7]. However, their scarcity and high industrial cost surely hinder the large-scale applications [8,9]. Therefore, it is highly imperative to design and develop efficient OER electrocatalysts with abundance or cost-effectiveness, such as noble-metal-free or low-content noble metal-based electrocatalysts [6,10–12].

Transition metal phosphides (TMPs) with comparable activity and sustainable stability have shown significant potential as alternatives to the commercial benchmark precious metal-based catalysts, making TMPs particularly promising for overall water electrolysis applications [4]. Specifically, binary TMPs, such as Ni_2P, CoP, and Fe_2P, are considered to be an important class of OER catalysts with approximate zero-valent metallic feature, high stability, and low cost, whose OER activities even exceed that of corresponding oxides/hydroxides [10,13–15]. This may be attributed to the gradual formation of catalytically active metal oxide/hydroxide phases on the TMPs surface during OER process, while the inner TMPs core imposes metal conduction properties to further facilitate electron transport [16,17]. Their intrinsic OER activity is closely related to the binding strength between the metal cation sites on their surfaces and the OER intermediates (*O, *OH, and *OOH). Therefore, regulating the electronic structure of the metal

* Corresponding authors.
E-mail addresses: lixiaowei419@shu.edu.cn (X. Li), Jinqiang.zhang@uts.edu.au (J. Zhang), Yufei.zhao@uts.edu.au (Y. Zhao), hao.liu@uts.edu.au (H. Liu).
[1] These authors contributed equally to this work.

https://doi.org/10.1016/j.jechem.2025.05.021

cations, specifically the number of 3*d* electrons that occupy the e_g orbital, can highly influence the corresponding OER catalytic capability. Incorporating an additional metal species into TMPs can induce synergistic effects between the different metal components, which can optimize the electronic properties of metal species, leading to charge redistribution and optimized binding affinities for reactants/intermediates. For instance, A ternary TMP ($Ni_{0.6}$-$Co_{1.4}P$ nanocages) achieved a current density of 10 mA cm^{-2} requiring an overpotential of 300 mV, significantly lower than those of Ni_2P (420 mV) and CoP (370 mV), which is caused by Co substitution improving more active sites exposure, stimulating charge redistribution and faster charge transfer [10]. In addition, Fe doped Ni_2P $(Ni_{0.5}Fe_{0.5})_2P$ effectively altered the electronic structure of Ni_2P and optimized the OH^- trapping and O_2 desorption, exhibiting more enhanced OER performance (overpotential of 219 mV at 20 mA cm^{-2}) than that of Ni_2P (261 mV) [18]. Notably, the engineered TMPs with synergistic effects have exhibited enhanced adsorption capabilities and remarkable reaction kinetics for OER; nevertheless, upgrading TMPs with satisfactory OER performance is still of great challenge.

Combining the transition metal phosphides with low-loading precious metals, especially the sub-nanometer structure or single atom, may present a promising strategy to utilize their individual advantages and achieve boosted OER catalytic performance [19]. The incorporated precious metal (e.g., Ru) with high intrinsic activity and stability can not only provide more active sites for OER, but also engineer the properties of transition metals. For instance, Fe–O (P) bonding strengthened by the incorporation of Ru single atom into FeP_4/Fe_2PO_5 nanosheets, coupled to the true active site Ru–O, lowered adsorption energy barriers to oxygen-containing intermediates and accelerated the water decomposition process [20]. Hollow Ru-incorporated Co_xP polyhedron underwent partial oxidative reconstitution during OER to form Ru/RuO_2 and Co_xP/CoOOH core-shell structures, and these multiple centers cooperated as the actual surface-active sites to provide outstanding OER activity and stability [21]. Moreover, some studies have demonstrated that the OER activity of TMPs can be enhanced after Ru introduction with the transition metal sites rather than the Ru sites dominating the OER process. Ru dopants modified the electronic structure of NiCoP nanowires, regulating the adsorption capacity of intermediates and promoting OER activity. Meanwhile, the formation of oxyhydroxides (NiOOH/CoOOH) on the nanowire surface during the OER process is believed to provide the actual active sites for the reaction [22]. Therefore, it is highly important to design stable and efficient TMP-based catalysts by integrating an effective structure and strategically Ru doping to enhance OER performance.

Herein, we have designed RuP-NiFeP composed of RuP_4 clusters anchored on porous NiFeP nanosheets for highly efficient OER. The porous nanosheet architecture is conducive to the exposure of active sites and mass transfer. The formed Ru-P/O-Ni/Fe bridges between RuP_4 clusters and NiFeP nanosheets trigger electron redistribution among Ru, Ni, and Fe atoms to optimize the adsorption energies of reactant/intermediates during OER process. Moreover, the RuP_4 clusters not only serve as OER catalytic active sites, but also induce structural evolution to form the disorder γ-NiOOH, which synergistically enhances the OER performance. The operando measurements and density functional theory (DFT) calculations have been conducted to reveal that the Ru incorporation converts the OER mechanism from the absorbate evolution mechanism (AEM) pathway (NiFeP) to the lattice oxygen mechanism (LOM) pathway in RuP-NiFeP with *OH deprotonation as rate-determining step (RDS). This allows RuP-NiFeP to achieve remarkable OER performance and stability, requiring an overpotential as low as 225 mV to achieve the current density of 100 mA cm^{-2} and maintaining a current retention rate of up to 98.1% after 24 h at 50 mA cm^{-2}. This work provides new insights into the development of highly efficient TMP-based OER catalysts, along with an in-depth investigation and analysis of the underlying mechanisms, offering valuable guidance for future research in catalyst design.

2. Experimental

2.1. Preparation of NiFe-LDH

Hydrothermal technique was employed to prepare NiFe-LDH. Typically, a clean and dry nickel foam (NF) (4 cm × 1 cm) was obtained by ultrasonic treatment with 3 M HCl solution, acetone, ethanol, and deionized water in sequence, followed by drying in a vacuum oven at 60 °C for 8 h. $NiCl_2$ (1 mmol), $FeCl_3$ (0.3 mmol), and urea (3 mmol) were added to a mixture of methanol (58 mL) and deionized water (2 mL), followed by ultrasonic process to obtain a clear solution. Subsequently, the above clarified mixture containing the treated NF was transferred to a Teflon-lined stainless autoclave and heated at 120 °C for 12 h. The NiFe-LDH was obtained after washing several times with deionized water and ethanol and drying in a vacuum oven overnight. Ni-LDH and Fe-LDH were prepared via the same procedure as NiFe-LDH without addition of $FeCl_3$ and $NiCl_2$, respectively.

2.2. Preparation of RuNiFe-LDH

RuNiFe-LDH was obtained by repeatedly impregnating NiFe-LDH into ethanol solution (5 mL) containing ruthenium acetylacetone (7 mmol). In particular, the impregnation-drying process was alternated 10 times. RuNi-LDH and RuFe-LDH were synthesized via the same procedure.

2.3. Preparation of RuP-NiFeP

Solid-state phosphorization treatment was used to develop RuP-NiFeP. Briefly, $NaH_2PO_2{\cdot}H_2O$ and RuNiFe-LDH were placed upstream and downstream of the tube furnace respectively in a mass ratio of 5:1. They were maintained at 300 °C for 2 h in an inert atmosphere, with a heating rate is 5 °C min^{-1}. NiFeP, RuP-NiP, and RuP-FeP were synthesized via the same procedure.

3. Results and discussion

3.1. Structural characterization

We constructed RuP-NiFeP through a multi-step impregnation strategy followed by solid-phase phosphorylation (Fig. 1a). Typically, NiFe-LDH on Ni foam was prepared via the hydrothermal method. Ru was introduced to the NiFe-LDH by a wet impregnation process, which resulted in RuNiFe-LDH two-dimensional (2D) nanosheets on Ni foam (Fig. S1). The transmission electron microscopy (TEM) images of NiFe-LDH and RuNiFe-LDH in Fig. S1 show the 2D nanosheets structure, and the corresponding elemental mapping results reveal the uniform distribution of Fe and Ni elements in NiFe-LDH and Fe, Ni, and Ru in RuNiFe-LDH, demonstrating the successful incorporation of Ru in RuNiFe-LDH and that this strategy has no influence on the original nanosheets structure. RuP-NiFeP was achieved through a solid-phase phosphorylation procedure on RuNiFe-LDH, which is verified by the appearance of a new peak at 40.8° in the X-ray diffraction (XRD) pattern of RuP-NiFeP compared to those of NiFe-LDH and RuNiFe-LDH (Fig. S2). This peak corresponds to (1 1 1) plane of Ni_2P (JCPDS: 03-0953), suggesting the successful phosphating treatment on RuNiFe-LDH. No peaks attributed to RuP_4 were detected, probably

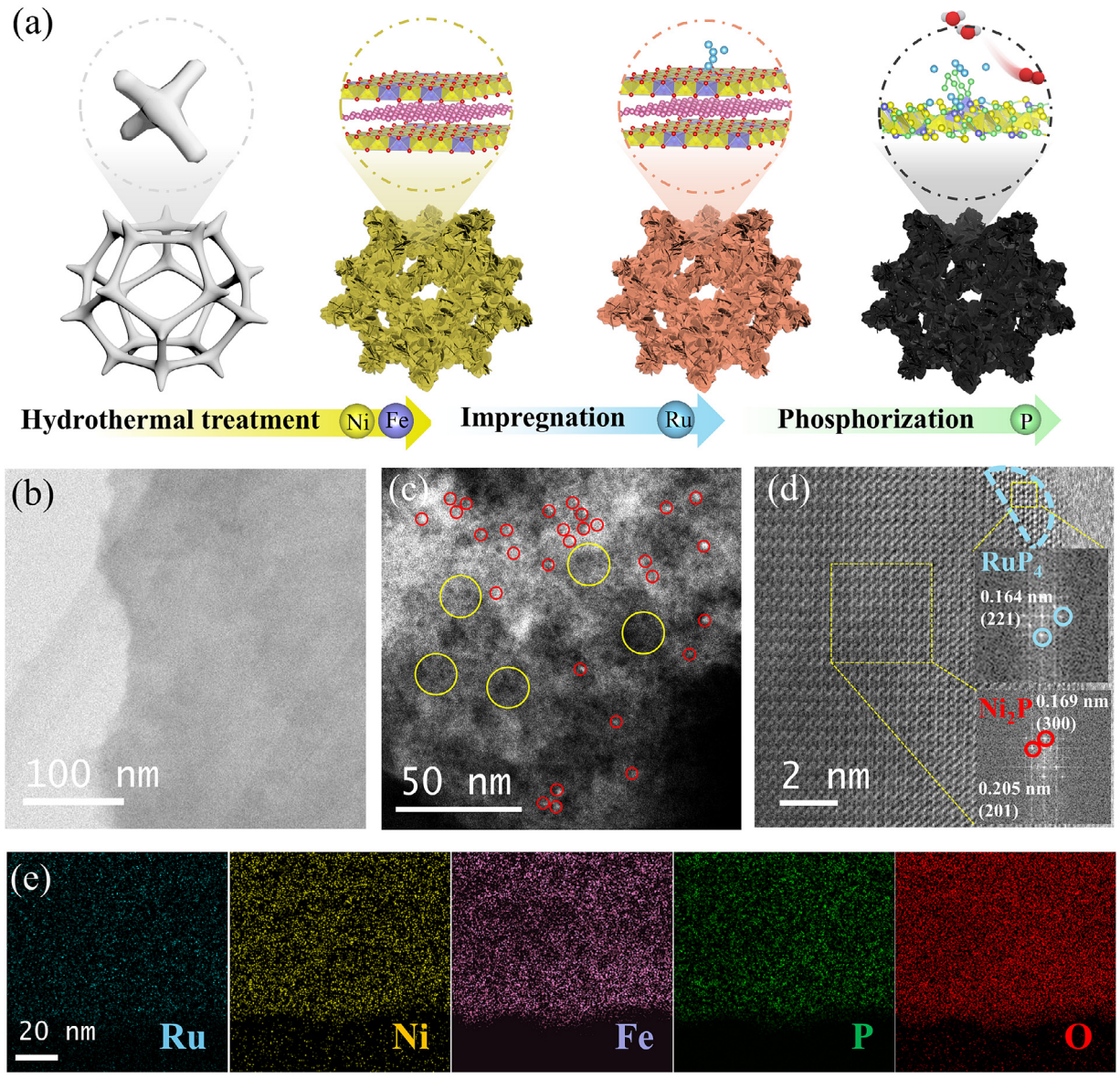

Fig. 1. (a) Schematic illustration of the synthetic procedure of RuP-NiFeP. (b) TEM, (c) HAADF-STEM, and (d) zoom-in HAADF-STEM images of RuP-NiFeP. (e) Elemental mapping images of RuP-NiFeP.

due to the low content of Ru. The TEM image shows that RuP-NiFeP maintains a 2D nanosheet structure (Fig. 1b). The high-angle annular dark field scanning transmission electron microscopy (HAADF-STEM) image reveals many tiny pores on the nanosheets (yellow circles), which are beneficial to active site exposure and electrolyte penetration. Moreover, numerous brighter clusters (red circles) with an average diameter of 1.84 nm are spotted on the nanosheets (Fig. 1c and Fig. S3). The zoom-in HAADF-STEM image in Fig. 1(d) clearly demonstrates a cluster with a diameter of ~2 nm immobilized on the nanosheets. The fast Fourier transform patterns in the inset of Fig. 1(d) reveal that the cluster corresponds to RuP_4 and the nanosheet is Ni_2P. The slightly larger lattice is attributed to the Fe doping, which enlarges the interplane spacing [23]. Furthermore, the electron energy loss spectroscopy (EELS) elemental mapping results in Fig. 1(e) decipher that the Ru, Ni, Fe, P, and O atoms are uniformly dispersed throughout RuP-NiFeP nanosheets, further verifying the successful preparation of RuP_4 clusters on NiFeP nanosheets with uniform distribution. We have also synthesized NiFeP, RuP-NiP, and RuP-FeP nanosheets as comparison samples. The XRD patterns (Fig. S4) of NiFeP, RuP-NiP, and RuP-FeP show similar peak position to that of RuP-NiFeP, confirming the successful preparation of corresponding metal phosphides. The TEM images in Fig. S5 show that NiFeP, RuP-NiP, and RuP-FeP present analogous lamellar architectures to RuP-NiFeP.

X-ray photoelectron spectroscopy (XPS) and X-ray absorption spectroscopy (XAS) were employed to unravel the surface chemical states and coordination environment of RuP-NiFeP. As shown in Fig. 2(a), the high-resolution XPS spectra of Ru 3*p* for RuP-NiFeP exhibit that the peaks of Ru $3p_{3/2}$ and Ru $3p_{1/2}$ are located at 462.3 and 484.3 eV, with a slightly positive shift of 0.34 and 0.41 eV compared to RuP-NiP and RuP-FeP, respectively, revealing the electron transfer from Ru to M (Ni or Fe) through the Ru–P/O–M bond [24]. Especially, more charge transfer occurred between Ru and Ni than between Ru and Fe. In addition, the binding energy of Ru $3p_{3/2}$ of RuP-NiFeP electrocatalyst is higher than 461.7 eV (Ru^0 $3p_{3/2}$) and lower than 463.1 eV (Ru^{III} $3p_{3/2}$), proving that the

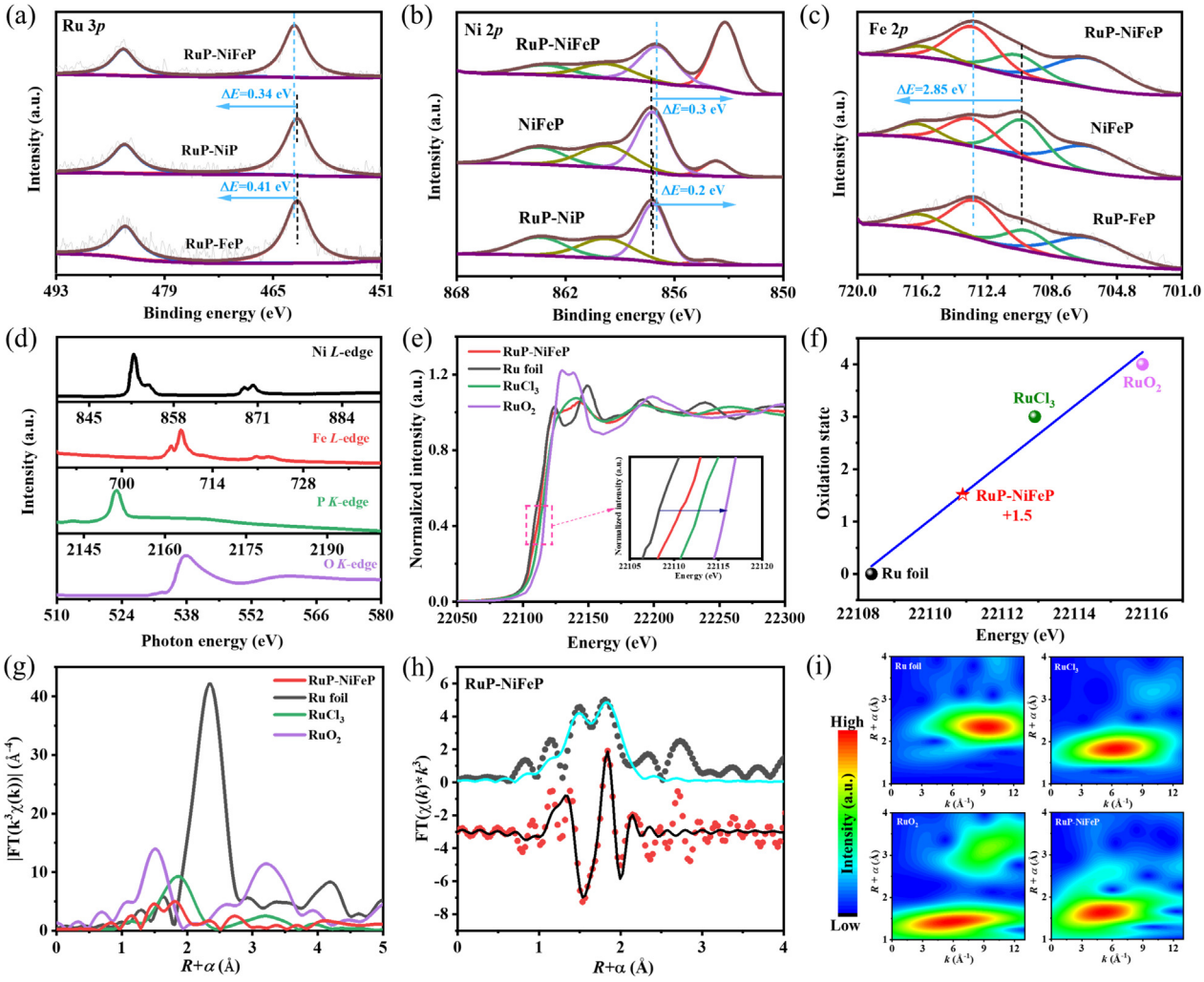

Fig. 2. High-resolution XPS spectra of (a) Ru 3*p*, (b) Ni 2*p*, and (c) Fe 2*p* of catalysts. (d) Near-edge XAFS spectra of Ni *L*-edge, Fe *L*-edge, P *K*-edge, and O *K*-edge of RuP-NiFeP. (e) Ru *K*-edge XANES spectra, the inset is the magnified pre-edge XANES region. (f) Calculated Ru valence states from the difference in XANES spectra. (g) FT k^3-weighted $\chi(k)$-function of the EXAFS spectra for the Ru *K*-edge. (h) The fitting of FT *R*-space Ru *K*-edge EXAFS of RuP-NiFeP. (i) The corresponding WT of the k^3-weighted Ru *K*-edge EXAFS signal of Ru foil, RuO_2, $RuCl_3$, and RuP-NiFeP.

valence state of Ru in RuP-NiFeP is between 0 and +3 [25,26]. The Ni 2*p* spectra of RuP-NiFeP, NiFeP, and RuP-NiP in Fig. 2(b) show that four peaks located at ~853.1, ~857.0, ~860.0, and ~863.3 eV are assigned to Ni–P, Ni^{3+}, Ni^{2+}, and satellite Ni, respectively [27–29]. Notably, compared with NiFeP and RuP-NiP, the Ni $2p_{3/2}$ peak of RuP-NiFeP is slightly shifted negatively by 0.3 and 0.2 eV respectively. It has been proved that electrons have been transferred from Ru/Fe to Ni. Similarly, the high-resolution XPS spectra of Fe 2*p* for RuP-NiFeP in Fig. 2(c) are deconvolved into four peaks, assigned to Fe–P (~707 eV), Fe^{3+} (~710 eV), Fe^{2+} (~713 eV), and satellite Fe (~717 eV) [29]. The Fe $2p_{3/2}$ peak of RuP-NiFeP exhibits a notable positive shift (~2.9 eV) compared to NiFeP, demonstrating that Ru incorporation induces electron redistribution, where charge transfer from Fe to Ni exceeds that from Ru to Fe. This electron configuration elevates Fe to a more oxidized state [30]. In the OER process, the elevated valence of Fe promotes potential-dependent structural evolution of Ni species, which is conducive to bonding with OH^-, thereby effectively enhancing water dissociation kinetics in the alkaline electrolyte [31]. In addition, the P 2*p* spectrum (Fig. S6) demonstrates the presence of P–O bond (~134 eV) and phosphorus anions in metal phosphides (~130.5 and ~129.5 eV), where the P–O bond is attributed to oxidation in the exposed air or doping during phosphating [32]. The O 1*s* spectrum displays the formation of M–O bond (Fig. S6). The XPS analysis reveals an efficient charge transfer pathway from Ru to the Ni/Fe in the RuP-NiFeP, as evidenced by the distinct binding energy shifts of Ru, Ni, and Fe species, demonstrating strong interaction between the RuP_4 clusters and NiFeP substrate.

The results of soft XAS in Fig. 2(d) show that the valence state of Ni species in RuP-NiFeP is dominant as +2 and that of Fe species is +3 valence state [33,34], which is consistent with the XPS results. The P *K*-edge peak at ~2151 eV and the O *K*-edge peak at ~538 eV represent the energy positions of the PO_4^- group and P 3*sp*-O 2*p* hybrid states, respectively, which may be derived from the oxidation of M–P bond in the exposed air [35]. The Ru *K*-edge of X-ray absorption near-edge structure (XANES) spectra in Fig. 2(e) shows that the absorption edge position of RuP-NiFeP is between Ru foil and $RuCl_3$, indicating that the oxidation state of Ru element in RuP-NiFeP is between 0 and +3 [26]. We further calculate the oxidation state of Ru by fitting the edge energy, and the calculated average valence state of Ru is around +1.5 (Fig. 2f) [36]. The Fourier transformed (FT) k^3-weighted extended X-ray absorption fine structure (FT-EXAFS) spectra of Ru for RuP-NiFeP deliver two dominant peaks at ~1.5 and ~1.8 Å, which are ascribed to

Ru–O and Ru–P bonds, respectively (Fig. 2g). No obvious peak appears at ~2.3 Å belonging to the Ru–Ru bond, proving the absence of metallic Ru [6,37]. The fitting EXAFS results of the *R*-space spectrum elucidate the coordination between Ru, O, and P, further confirming that each Ru atom is coordinated with 0.68 O atom and 2.9 P atoms in RuP-NiFeP (Fig. 2h, Fig. S7 and Table S1). Wavelet transform (WT) EXAFS spectrum presents maximum signal intensity of RuP-NiFeP at ~5 Å, which is significantly different from that of Ru, but similar to that of $RuCl_3$ and RuO_2, supporting the absence of Ru metal and the presence of Ru-light atoms (Fig. 2i). Combining the results of XPS and XAS, Ru-P/O-TM bridges were constructed between the RuP_4 cluster and the NiFeP substrate. It allows for the directional transfer of electrons from RuP_4 to NiFeP, thereby optimizing the electronic structure of RuP-NiFeP and endowing it with excellent OER catalytic activity.

3.2. Electrochemical performance

The OER electrocatalytic performance of the as-obtained samples was examined in 1.0 M KOH solution through a typical three-electrode system. As shown in Fig. 3(a) and Fig. S8, NiFe-LDH, RuNiFe-LDH, and RuP-NiFeP exhibit an increased activity trend for OER. Moreover, RuP-NiFeP also delivers lower Tafel slope and impedance compared to NiFe-LDH and RuNiFe-LDH, indicating that the phosphating step indeed boosts the corresponding OER catalytic capability. As shown in Fig. 3 and Fig. S9, RuP-NiFeP also delivers superior OER activity with the smallest overpotential of 225 mV to achieve a current density of 100 mA cm^{-2}, compared to those of NiFeP (254 mV), RuP-NiP (319 mV), and RuP-FeP (295 mV). Tafel analysis further demonstrates that RuP-NiFeP possesses excellent OER kinetics with a lower Tafel slope of 27.4 mV dec^{-1} than NiFeP (61.1 mV dec^{-1}), RuP-FeP (44.2 mV dec^{-1}), and RuP-NiP (101.5 mV dec^{-1}) (Fig. 3b). Additionally, the OER performance of RuP-NiFeP exceeds that of most reported TMP-based electrocatalysts as shown in Fig. 3(c) and Table S2. We further conducted cyclic voltammetry (CV) at different scan rates in non-Faradaic regions to investigate double-layer capacitance (C_{dl}) and electrochemical active area (ECSA) (Fig. S10). RuP-NiFeP shows the largest C_{dl} of 5.04 mF cm^{-2} and ECSA of 2.52 cm^2, respectively (Fig. 3d and Fig. S10), implying more exposed active sites for OER [6,38]. After normalizing current density by the ECSA, RuP-NiFeP still exhibits the smallest overpotential of 230 mV at 100 mA cm^{-2} (Fig. S11) among all samples (265 mV for NiFeP, 333 mV for RuP-NiP, and 336 mV for RuP-FeP), verifying the outstanding inherent OER activity. This demonstrates that the integration of Ru and the construction of Ru-P/O-TM bridge promoting electron transfer are conducive to the formation and exposure of highly efficient active sites, showing high OER kinetics. Furthermore, electrochemical impedance spectra (EIS) are performed to reveal the interface resistance [38]. The results in Fig. 3(e) suggest RuP-NiFeP with the smallest semi-circle compared to NiFeP, RuP-FeP, and RuP-NiP, indicating that RuP-NiFeP has pronounced conductive properties and fast charge transfer capability thanks to the Ru-P/O-TM bridge [6]. The OER durability of RuP-NiFeP was investigated by chronoamperometry *i-t* test at 50 mA cm^{-2} and the result shows a negligible current drop with a retention rate of 98.1% after continuous operation for 24 h (Fig. 3f). Moreover, the linear sweep voltammetry (LSV) curves of RuP-NiFeP show imperceptible variation before and after the *i-t* test, further demonstrating the excellent stability of RuP-NiFeP for OER.

3.3. Understanding of the catalytic mechanism

The superior OER catalytic activity of RuP-NiFeP should be attributed to the strong interactions between Ru-based clusters and metal phosphide, which causes the spatial electron redistribution beneficial to optimizing the absorption energy of the OER

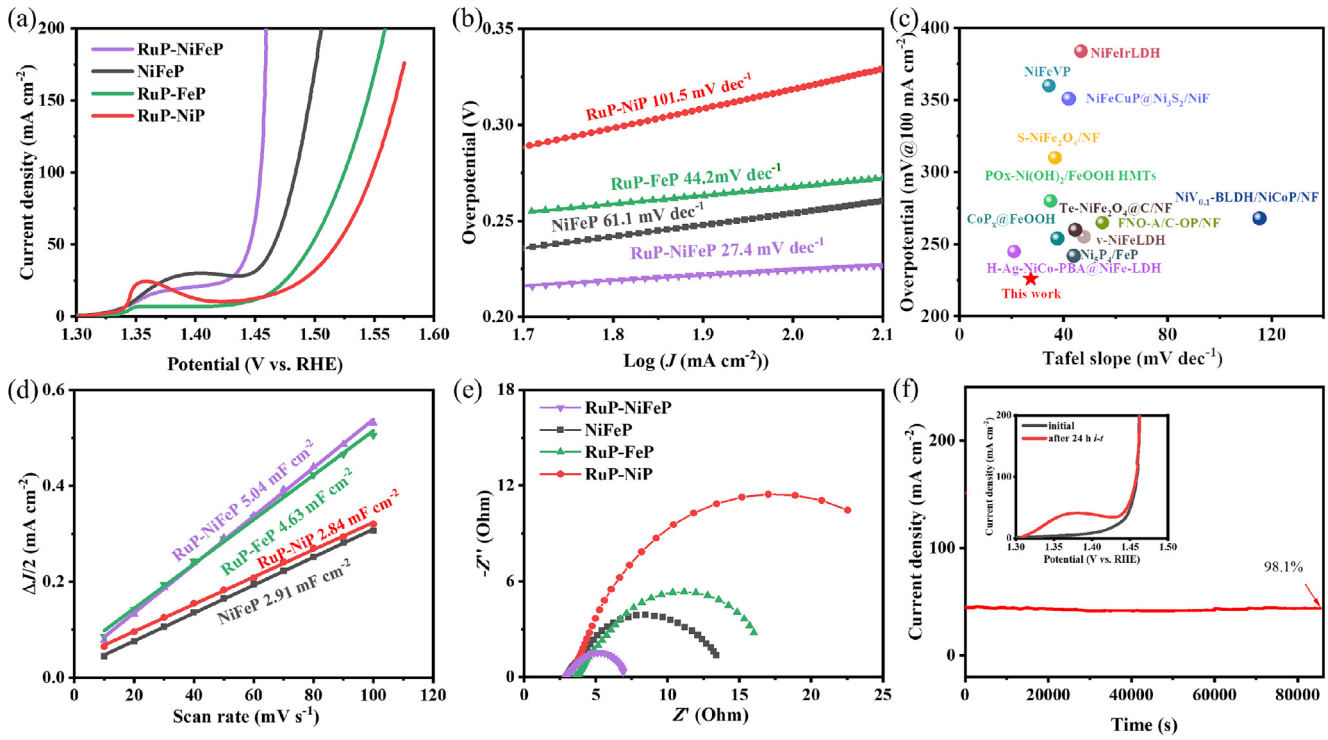

Fig. 3. (a) LSV curves of different catalysts for OER and (b) corresponding Tafel plots. (c) The comparison of overpotential and Tafel slope at the current density of 100 mA cm^{-2} between RuP-NiFeP and the reported catalysts. (d) C_{dl} extracting from the CV curves. (e) EIS Nyquist plots of catalysts measured at 1.43 V vs. RHE. (f) Chronoamperometry *i-t* test of RuP-NiFeP at 50 mA cm^{-2}. The inset is LSV curves before and after *i-t* test of RuP-NiFeP.

intermediates and promoting the OER process. In order to further investigate the catalytic mechanism of RuP-NiFeP for OER process, tetramethylammonium cation (TMA^+) was used as a chemical probe to detect negatively charged oxygenated intermediates ($^*O_2^{2-}$ or $^*O_2^-$) produced during OER based on their specific electrostatic interaction [39]. As shown in Fig. 4(a) and Fig. S12, the OER activity of RuP-NiFeP decreased significantly with the Tafel slope of 27.4 mV dec^{-1} increasing to 59.1 mV dec^{-1} after replacing KOH with tetramethylammonium hydroxide (TMAOH), which should be attributed to the electrostatic interaction between TMA^+ and the negatively charged oxygenated intermediates, competing with the OER process. As $^*O_2^{2-}$ or $^*O_2^-$ is generated in the LOM route, the decreased catalytic activity in TMAOH indicates RuP-NiFeP following the LOM pathway in the OER process. The activity decay phenomena have been also observed for RuP-NiP and RuP-FeP (Fig. S13), indicating that they also follow the LOM catalytic mechanism, whereas almost no catalytic activity change occurred for NiFeP (Fig. 4b), suggesting that the reactions on NiFeP follow AEM for OER. The above results indicate that the OER catalytic pathway has shifted from AEM to LOM due to the incorporation of Ru species. In addition, the catalytic mechanism has also been investigated by pH dependence measurements to evaluate the dependence of OER reaction kinetics of catalysts on proton activity [40]. The results in Fig. 4(c, d) and Fig. S14 show that the OER catalytic activities of RuP-NiFeP, NiFeP, RuP-FeP, and RuP-NiP are all proportional to pH value. Specifically, the OER activity of RuP-NiFeP was promoted significantly with increasing pH, showing a strong pH dependence, indicating that the kinetics of OER may be limited by non-concerted proton and electron transfer processes (NCPET), which is an important signal of LOM process [41]. In addition, the proton reaction order ρ^{RHE} representing the degree of coupling between proton and electron transfer during OER process was calculated, and the result confirms that RuP-NiFeP (ρ^{RHE} = 1.42) delivers the highest degree of decoupled proton-electron transfer among all the samples (ρ^{RHE} values of NiFeP, RuP-FeP, and RuP-NiP are 1.06, 1.24, and 0.64, respectively), that is, the RDS of OER on RuP-NiFeP is the chemical deprotonation step (Fig. S14) [42]. Ru incorporation makes the OER on RuP-NiFeP follow the LOM pathway with deprotonation as the RDS, which is in agreement with the conclusions of the above test of TMAOH as the OER electrolyte. The presence of LOM pathway breaks the linear relation between *OH and *OOH intermediates in AEM, allowing for a lower overpotential of 225 mV at 100 mA cm^{-2} for RuP-NiFeP during OER, much superior to the typical 370 mV at 10 mA cm^{-2} for AEM pathway [43].

The operando measurements have been conducted to further investigate the catalytic mechanism. The results of in situ Fourier

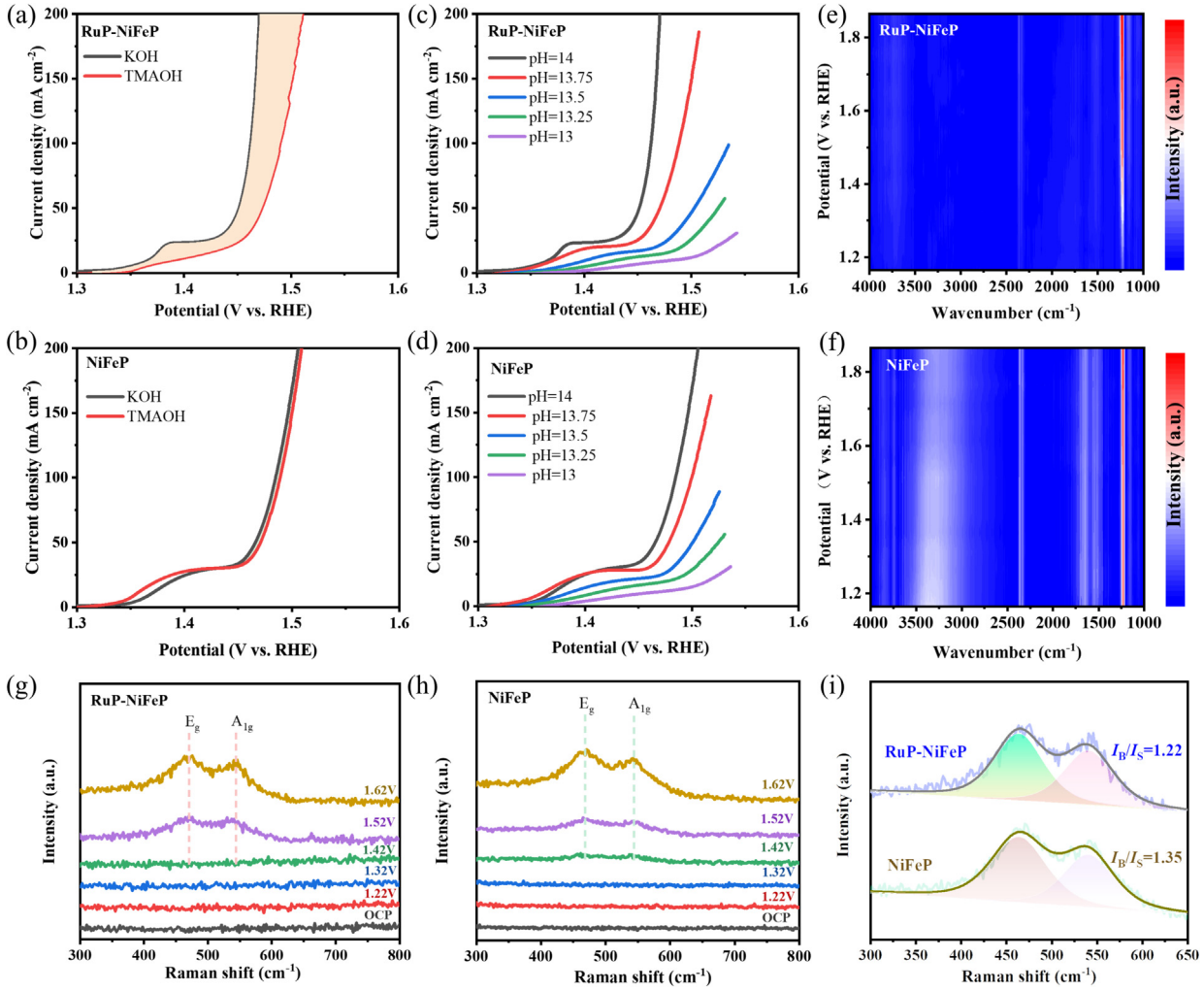

Fig. 4. LSV curves of (a) RuP-NiFeP and (b) NiFeP in 1.0 M KOH and 1.0 M TMAOH, respectively. LSV curves of (c) RuP-NiFeP and (d) NiFeP in electrolytes with different pH values. In situ FTIR spectrum of (e) RuP-NiFeP and (f) NiFeP. In situ Raman spectra of (g) RuP-NiFeP and (h) NiFeP. (i) Raman spectra collected at 1.65 V (vs. RHE) and the responding I_B/I_S value.

transform infrared (FTIR) spectroscopy for NiFeP and RuP-NiFeP are illustrated in Fig. 4(e, f). Generally, peaks at ~3300, ~1650, 1250–1120 [44], and 1200–1010 cm^{-1} [45] correspond to the infrared vibration peaks of the surface-adsorbed OH_{ads}, O, OOH_{ads}, and the free superoxide species (O_2^-), respectively. Only two potential-dependent peaks appeared in the in situ FTIR spectroscopy of RuP-NiFeP at ~1230 and ~1150 cm^{-1}, which are assigned to the O–O stretching mode of OOH_{ads} [46,47] and the stretching mode of O_2^- [48,49], respectively. Especially, the appearance of O_2^- intermediates signifies that RuP-NiFeP follows the LOM pathway for OER. In contrast, adsorbed O (M–O) at ~1650 cm^{-1}, OH_{ads} (M–OH_{ads}) at ~3300 cm^{-1}, and OOH_{ads} at ~1230 cm^{-1} (M–OOH_{ads}) observed in Fig. 4(f) represent three typical intermediates of AEM pathway, revealing that NiFeP follows the AEM pathway [50]. The result further demonstrates that the incorporation of Ru species in metal phosphide induces the catalytic mechanistic shift from AEM to LOM, which may be responsible for the enhanced OER activity.

Meanwhile, in situ Raman spectroscopy was scrutinized to further investigate the interfacial phase evolution of the catalysts during the OER process. Fig. 4(g and h) shows that no obvious peak can be observed in Raman spectra of both NiFeP and RuP-NiFeP collected under open circuit conditions. However, two detectable Raman bands at ~464 and ~540 cm^{-1} appear with the increase of potential, ascribed to the bending vibration (E_g) and stretching vibration (A_{1g}) of Ni–O, respectively, revealing the formation of γ-NiOOH phase, which is usually the active phase for OER [51,52]. No obvious bands associated with FeOOH or Ru–O were detected in Raman spectra, maybe resulting from the relatively low content [6]. Notably, the Ni–O stretching and bending bands (464 and 540 cm^{-1}) in both RuP-NiFeP (Fig. 4g) and NiFeP (Fig. 4h) have a red-shift of more than 10 cm^{-1} compared to pure γ-NiOOH (bands centered at 477 and 557 cm^{-1}), which is attributed to the elongation of the Ni–O bonds generated by Fe incorporation [53,54]. Additionally, the applied potential of γ-NiOOH phase appearing in the Raman spectrum of RuP-NiFeP (1.52 V vs. RHE) is slightly higher than that of NiFeP (1.42 V vs. RHE), which may be due to that the introduction of Ru hampers the generation of high-valent $Ni^{\delta+}$ and delays the formation of γ-NiOOH [55]. This aligns with the XPS analysis showing that Ru promotes the shift of Ni toward a reduced state, thereby unfavorable for the formation of Ni in an oxidized state. Therefore, the remarkable OER activity of RuP-NiFeP under a low potential could potentially stem from the contribution of Ru species [31]. Furthermore, the intensity ratio of E_g band and A_{1g} band (I_B/I_S) related to the structural disorder of the NiOOH phase is generally adopted to indicate the OER activity [53,55]. As depicted in Fig. 4(i), the I_B/I_S value of RuP-NiFeP (1.22) is lower than that of NiFeP (1.35), demonstrating more disordered γ-NiOOH phase formed due to the presence of Ru species. The disordered γ-NiOOH may synergistically act as the active sites together with Ru species to achieve promoted OER activity [53], that is, under low-potential conditions, the Ru sites act as active centers to drive OER, while at higher potentials, Ru and Ni sites synergistically collaborate to further enhance the OER process.

To further elucidate the active sites and reaction thermodynamics of RuP-NiFeP during OER process, DFT calculations were performed. Based on the structural dynamic evolution from in situ Raman results, the structural model of RuP/NiFeOOH (shown in Fig. S15) representing RuP-NiFeP was established to reveal the origin of OER activity. The charge density difference of RuP/NiFeOOH was first investigated, which shows the electron transfer from RuP_4 cluster to NiFeOOH through Ru-P/O-TM bridge, leading to the spatial electron redistribution on Ru and Ni/Fe species (Fig. 5a), which is consistent with the XPS and XAS results. Moreover, the projected

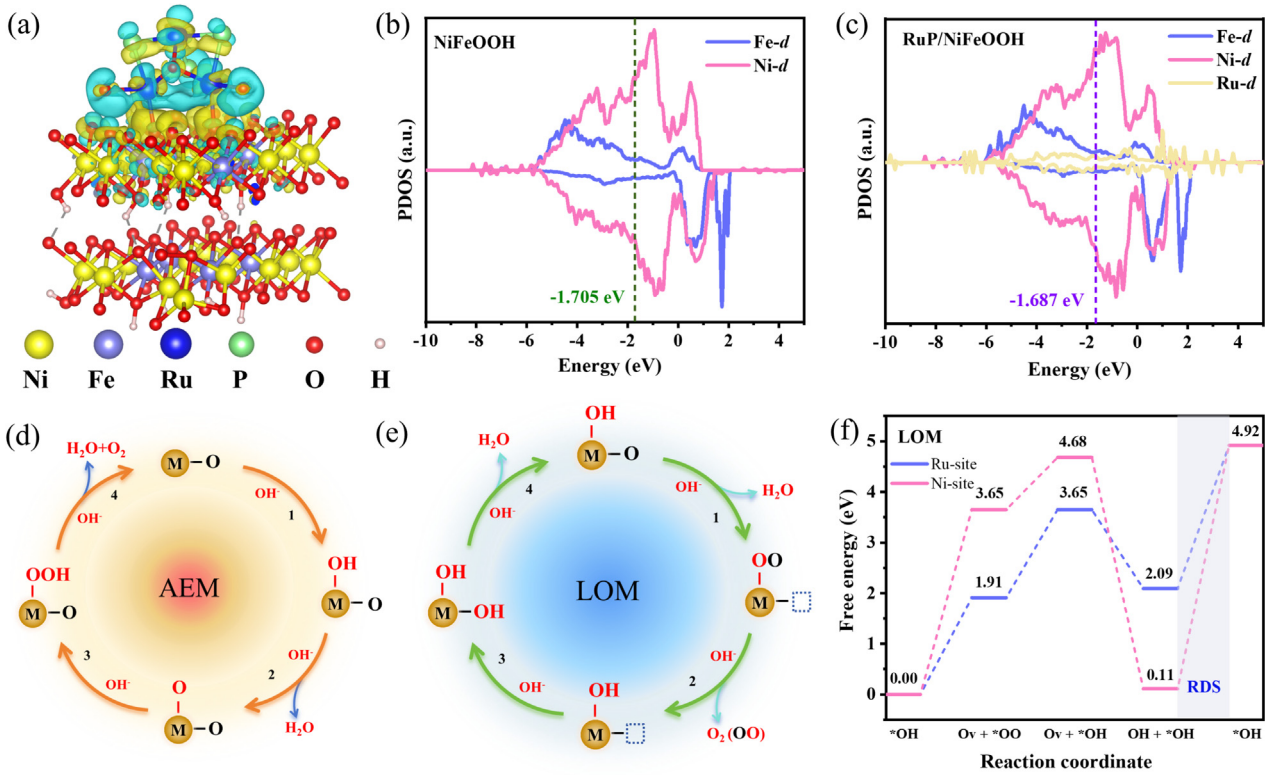

Fig. 5. (a) The charge density difference of the RuP/NiFeOOH (the yellow and light blue areas represent accumulation and charge depletion, respectively). The PDOS for (b) NiFeOOH and (c) RuP/NiFeOOH. The schematic illustration of (d) AEM pathway and (e) LOM pathway. (f) Calculated Gibbs free energy diagram of OER following LOM at the Ru site and Ni site on the surface of RuP/NiFeOOH.

density of states (PDOS) in Fig. 5(b and c) reveals a relatively higher *d*-band center near the Fermi level in RuP/NiFeOOH (−1.687 eV) compared to NiFeOOH (−1.705 eV), indicating that the incorporation of Ru promotes electron delocalization and enhances the conductivity of RuP/NiFeOOH [56,57]. This enables effective electron transfer between Ru/Ni sites and intermediates, thus improving the OER process [58].

Generally, AEM and LOM represent the predominant reaction pathways for OER occurring on surfaces of the electrocatalyst. The formation and conversion of intermediates *OH, *O, and *OOH are characteristic of the AEM pathway, while the direct coupling of the O–O bond represents a distinctive feature of the LOM pathway (Fig. 5d, e) [58,59]. For AEM, the *OH and *OOH binding energies (ΔG_{*OOH} and ΔG_{*OH}) scale linearly with a constant energy difference of ca. 3.2 eV, meaning that a minimum theoretical overpotential is 370 mV [60]. LOM bypasses the scaling relations limitations of AEM, enabling reduced overpotentials in OER. Combined with the results of in-situ characterization and mechanism exploration experiments, RuP-NiFeP may undergo LOM pathway during OER process. To further determine the active sites for OER, both Ru and Ni sites in RuP/NiFeOOH were scrutinized following the LOM pathway. Fig. 5(f) presents the Gibbs free energy diagram for OER through the LOM pathway on RuP/NiFeOOH, disclosing that the conversion from *OH to *O constitutes the RDS. Among them, Ru sites on RuP/NiFeOOH exhibit a lower overpotential (1.60 eV) compared to the Ni sites (3.58 eV), revealing that Ru sites are more likely to dominate the LOM pathway during the OER process, while Ni sites require a high potential to trigger OER. In addition, we further calculated the free energy changes for Ru sites following the AEM pathway during the OER process illustrated in Fig. S16, revealing that the formation of *OOH is the RDS with a relatively high overpotential of 2.88 eV. Consequently, above calculation results demonstrate that the OER preferentially proceeds via the LOM at the Ru sites in RuP/NiFeOOH with the deprotonation of *OH as RDS.

In summary, the Ru-P/O-TM bridge constructed after the introduction of Ru promotes electron transfer from Ru to Ni/Fe, optimizing the electronic structure of Ni/Fe and thereby enhancing the intrinsic activity and reaction kinetics of RuP-NiFeP. The synergistic collaboration between Ru and Ni active sites accelerates the OER process, breaking the linear scaling limitation in AEM pathway, favoring the LOM pathway, and ultimately exhibiting superior OER performance with lower overpotential.

4. Conclusions

We have developed an innovative RuP-NiFeP catalyst featuring RuP_4 cluster anchored on porous NiFeP nanosheets. The incorporation of Ru enables RuP-NiFeP to deliver highly efficient OER performance, achieving 100 mA cm^{-2} at a low overpotential of 225 mV, superior kinetics with a Tafel slope as low as 27.4 mV dec^{-1}, and excellent stability with a current retention rate up to 98.1% after 24 h at 50 mA cm^{-2}. The enhanced OER activity of RuP-NiFeP primarily stems from the increased exposure of active sites due to the porous nanosheet architecture and Ru incorporation, the modulated electronic structure via Ru-P/O-TM bridge, and the synergistic effect between Ru active sites and in-situ formed disordered Ni sites. Furthermore, electrochemical experiments, in situ techniques, and DFT calculations demonstrate that the integration of Ru drives a shift in the OER mechanism from the AEM pathway (characteristic of NiFeP) to the LOM pathway in RuP-NiFeP, along with the deprotonation of *OH identified as the RDS. This work offers novel perspectives on the development of highly efficient TMP-based OER catalysts, along with in-depth investigation and analysis of underlying mechanisms, serving as a foundation for future research endeavors.

CRediT authorship contribution statement

Fengying Pan: Writing – review & editing, Writing – original draft, Methodology, Formal analysis, Data curation, Conceptualization. **Cheng Gong:** Writing – review & editing, Writing – original draft, Formal analysis, Data curation. **Yiwen Sun:** Writing – review & editing, Software, Formal analysis. **Zeliang Wu:** Writing – review & editing, Formal analysis, Data curation. **Dongfang Li:** Writing – review & editing, Formal analysis, Data curation. **Jiaxin Wu:** Writing – review & editing, Formal analysis, Data curation. **Xianjun Cao:** Writing – review & editing, Supervision, Formal analysis, Data curation. **Yi Xu:** Writing – review & editing, Software, Methodology. **Xiaowei Li:** Methodology, Resources, Software, Writing – review & editing. **Hong Gao:** Writing – review & editing, Supervision, Resources. **Jinqiang Zhang:** Writing – review & editing, Funding acquisition, Formal analysis, Conceptualization. **Yufei Zhao:** Writing – review & editing, Supervision, Project administration, Funding acquisition, Conceptualization. **Hao Liu:** Writing – review & editing, Supervision, Funding acquisition, Conceptualization.

Declaration of competing interest

The authors declare that they have no known competing financial interests or personal relationships that could have appeared to influence the work reported in this paper.

Acknowledgments

This work was supported by the Australian Research Council (DE240100868), CSIRO "International Hydrogen Research Collaboration Program-RESEARCH FELLOWSHIPS", the National Natural Science Foundation of China (22209103), and the UTS Chancellor's Research Fellowships. Authors are grateful for support from the "Joint International Laboratory on Environmental and Energy Frontier Materials" and the "Innovation Research Team of High-Level Local Universities in Shanghai". This work was Supported by Shanghai Technical Service Center of Science and Engineering Computing, Shanghai University.

Appendix A. Supplementary material

Supplementary data to this article can be found online at https://doi.org/10.1016/j.jechem.2025.05.021.

References

[1] D. Wu, B. Liu, R. Li, D. Chen, W. Zeng, H. Zhao, Y. Yao, R. Qin, J. Yu, L. Chen, J. Zhang, B. Li, S. Mu, Small 19 (2023) 2300030.
[2] J. Guo, J. Huo, Y. Liu, W. Wu, Y. Wang, M. Wu, H. Liu, G. Wang, Small Methods 3 (2019) 1900159.
[3] N.-T. Suen, S.-F. Hung, Q. Quan, N. Zhang, Y.-J. Xu, H.M. Chen, Chem. Soc. Rev. 46 (2017) 337–365.
[4] Y. Li, Z. Dong, L. Jiao, Adv. Energy Mater. 10 (2020) 1902104.
[5] L. Xiu, W. Pei, S. Zhou, Z. Wang, P. Yang, J. Zhao, J. Qiu, Adv. Funct. Mater. 30 (2020) 1910028.
[6] X. Li, T. Wu, N. Li, S. Zhang, W. Chang, J. Chi, X. Liu, L. Wang, Adv. Funct. Mater. (2024) 2400734.
[7] M. Ledendecker, S. Krick Calderón, C. Papp, H. Steinrück, M. Antonietti, M. Shalom, Angew. Chem. Int. Ed. 54 (2015) 12361–12365.
[8] X. Zhou, Y. Zi, L. Xu, T. Li, J. Yang, J. Tang, Inorg. Chem. 60 (2021) 11661–11671.
[9] X. Cao, J. Huo, L. Li, J. Qu, Y. Zhao, W. Chen, C. Liu, H. Liu, G. Wang, Adv. Energy Mater. 12 (2022) 2202119.
[10] B. Qiu, L. Cai, Y. Wang, Z. Lin, Y. Zuo, M. Wang, Y. Chai, Adv. Funct. Mater. 28 (2018) 1706008.
[11] K. Bhunia, M. Chandra, S. Kumar Sharma, D. Pradhan, S.-J. Kim, Coord. Chem. Rev. 478 (2023) 214956.

[12] S. Fu, Y. Ma, X. Yang, X. Yao, Z. Jiao, L. Cheng, P. Zhao, Appl. Catal. B Environ. 333 (2023) 122813.
[13] Z. Li, X. Dou, Y. Zhao, C. Wu, Inorg. Chem. Front. 3 (2016) 1021–1027.
[14] Z. Xiao, Y. Wang, Y.-C. Huang, Z. Wei, C.-L. Dong, J. Ma, S. Shen, Y. Li, S. Wang, Energ. Environ. Sci. 10 (2017) 2563–2569.
[15] L. Yan, Y. Sun, E. Hu, J. Ning, Y. Zhong, Z. Zhang, Y. Hu, J. Colloid Interface Sci. 541 (2019) 279–286.
[16] X.-Y. Yu, Y. Feng, B. Guan, X.W. (David) Lou, U. Paik, Energ. Environ. Sci. 9 (2016) 1246–1250.
[17] L.-A. Stern, L. Feng, F. Song, X. Hu, Energ. Environ. Sci. 8 (2015) 2347–2351.
[18] J. Yu, G. Cheng, W. Luo, J. Mater. Chem. A 5 (2017) 11229–11235.
[19] J. Zhao, Y. Zhang, Y. Xia, B. Zhang, Y. Du, B. Song, H.-L. Wang, S. Li, P. Xu, Appl. Catal. B Environ. 328 (2023) 122447.
[20] W. Xia, M. Ma, X. Guo, D. Cheng, D. Wu, D. Cao, ACS Appl. Mater. Interfaces 15 (2023) 44827–44838.
[21] L. Wang, Q. Zhou, Z. Pu, Q. Zhang, X. Mu, H. Jing, S. Liu, C. Chen, S. Mu, Nano Energy 53 (2018) 270–276.
[22] M. Zhao, S. Zhang, Y. Hu, H. Xing, C. Li, W. Yuan, W. Sun, C. Guo, C.M. Li, Int. J. Hydrog. Energy 51 (2024) 998–1009.
[23] Y. Li, X. Wei, R. Pan, Y. Wang, J. Luo, L. Li, L. Chen, J. Shi, Energy Environ. Sci. 17 (2024) 4205–4215.
[24] Y. Yang, Q.-N. Yang, Y.-B. Yang, P.-F. Guo, W.-X. Feng, Y. Jia, K. Wang, W.-T. Wang, Z.-H. He, Z.-T. Liu, ACS Catal. 13 (2023) 2771–2779.
[25] D.J. Morgan, Surf. Interface Anal. 47 (2015) 1072–1079.
[26] Y. Hu, G. Luo, L. Wang, X. Liu, Y. Qu, Y. Zhou, F. Zhou, Z. Li, Y. Li, T. Yao, C. Xiong, B. Yang, Z. Yu, Y. Wu, Adv. Energy Mater. 11 (2021) 2002816.
[27] P. Jiang, Q. Liu, Y. Liang, J. Tian, A.M. Asiri, X. Sun, Angew. Chem. Int. Ed. 53 (2014) 12855–12859.
[28] L. Li, C. Chen, L. Chen, Z. Zhu, J. Hu, Environ. Sci. Technol. 48 (2014) 3372–3377.
[29] A.P. Grosvenor, S.D. Wik, R.G. Cavell, A. Mar, Inorg. Chem. 44 (2005) 8988–8998.
[30] L. Wu, L. Yu, F. Zhang, B. McElhenny, D. Luo, A. Karim, S. Chen, Z. Ren, Adv. Funct. Mater. 31 (2021) 2006484.
[31] Z. Qiu, C.-W. Tai, G.A. Niklasson, T. Edvinsson, Energ. Environ. Sci. 12 (2019) 572–581.
[32] D. Chen, H. Bai, J. Zhu, C. Wu, H. Zhao, D. Wu, J. Jiao, P. Ji, S. Mu, Adv. Energy Mater. 13 (2023) 2300499.
[33] P.S. Miedema, F.M.F. De Groot, J. Electron Spectrosc. Relat. Phenom. 187 (2013) 32–48.
[34] F. Massel, S. Ahmadi, M. Hahlin, Y.-S. Liu, J.-H. Guo, T. Edvinsson, H. Rensmo, L.-C. Duda, J. Electron Spectrosc. Relat. Phenom. 224 (2018) 3–7.
[35] T. Jenkins, J.A. Alarco, B. Cowie, I.D.R. Mackinnon, J. Power Sources 571 (2023) 233078.
[36] P. Li, M. Wang, X. Duan, L. Zheng, X. Cheng, Y. Zhang, Y. Kuang, Y. Li, Q. Ma, Z. Feng, W. Liu, X. Sun, Nat. Commun. 10 (2019) 1711.
[37] K. Wu, K. Sun, S. Liu, W. Cheong, Z. Chen, C. Zhang, Y. Pan, Y. Cheng, Z. Zhuang, X. Wei, Y. Wangg, L. Zheng, Q. Zhang, D. Wang, Q. Peng, C. Chen, Y. Li, Nano Energy 80 (2021) 105467.
[38] Y. Zhu, Y. Chen, Y. Feng, X. Meng, J. Xia, G. Zhang, Adv. Mater. 36 (2024) 2401694.
[39] S. Xin, Y. Tang, B. Jia, Z. Zhang, C. Li, R. Bao, C. Li, J. Yi, J. Wang, T. Ma, Adv. Funct. Mater. 33 (2023) 2305243.
[40] F. Wang, P. Zou, Y. Zhang, W. Pan, Y. Li, L. Liang, C. Chen, H. Liu, S. Zheng, Nat. Commun. 14 (2023) 6019.
[41] C. Jia, X. Xiang, J. Zhang, Z. He, Z. Gong, H. Chen, N. Zhang, X. Wang, S. Zhao, Y. Chen, Adv. Funct. Mater. 33 (2023) 2301981.
[42] Z.-F. Huang, S. Xi, J. Song, S. Dou, X. Li, Y. Du, C. Diao, Z.J. Xu, X. Wang, Nat. Commun. 12 (2021) 3992.
[43] X. Li, C. Deng, Y. Kong, Q. Huo, L. Mi, J. Sun, J. Cao, J. Shao, X. Chen, W. Zhou, M. Lv, X. Chai, H. Yang, Q. Hu, C. He, Angew. Chem. Int. Ed. 62 (2023) e202309732.
[44] R. Nakamura, A. Imanishi, K. Murakoshi, Y. Nakato, J. Am. Chem. Soc. 125 (2003) 7443–7450.
[45] W. Cheng, X. Zhao, H. Su, F. Tang, W. Che, H. Zhang, Q. Liu, Nat. Energy 4 (2019) 115–122.
[46] Y. Yao, S. Hu, W. Chen, Z.-Q. Huang, W. Wei, T. Yao, R. Liu, K. Zang, X. Wang, G. Wu, W. Yuan, T. Yuan, B. Zhu, W. Liu, Z. Li, D. He, Z. Xue, Y. Wang, X. Zheng, J. Dong, C.-R. Chang, Y. Chen, X. Hong, J. Luo, S. Wei, W.-X. Li, P. Strasser, Y. Wu, Y. Li, Nat. Catal. 2 (2019) 304–313.
[47] S. Nayak, I.J. McPherson, K.A. Vincent, Angew. Chem. Int. Ed. 57 (2018) 12855–12858.
[48] C. Lin, J.-L. Li, X. Li, S. Yang, W. Luo, Y. Zhang, S.-H. Kim, D.-H. Kim, S.S. Shinde, Y.-F. Li, Z.-P. Liu, Z. Jiang, J.-H. Lee, Nat. Catal. 4 (2021) 1012–1023.
[49] Y. Hao, S.-F. Hung, W.-J. Zeng, Y. Wang, C. Zhang, C.-H. Kuo, L. Wang, S. Zhao, Y. Zhang, H.-Y. Chen, S. Peng, Switching the oxygen evolution mechanism on atomically dispersed Ru for enhanced acidic reaction kinetics, J. Am. Chem. Soc. 145 (2023) 11.
[50] Y. Hu, Y. Zheng, J. Jin, Y. Wang, Y. Peng, J. Yin, W. Shen, Y. Hou, L. Zhu, L. An, M. Lu, P. Xi, C.-H. Yan, Nat. Commun. 14 (2023) 1949.
[51] J. Huang, Y. Li, Y. Zhang, G. Rao, C. Wu, Y. Hu, X. Wang, R. Lu, Y. Li, J. Xiong, Angew. Chem. Int. Ed. 58 (2019) 17458–17464.
[52] Z. Qiu, Y. Ma, T. Edvinsson, Nano Energy 66 (2019) 104118.
[53] Y. Li, Y. Wu, H. Hao, M. Yuan, Z. Lv, L. Xu, B. Wei, Appl. Catal. B Environ. 305 (2022) 121033.
[54] M. Chen, Y. Zhang, J. Chen, R. Wang, B. Zhang, B. Song, P. Xu, Small 20 (2024) 2309371.
[55] H. Hao, Y. Li, Y. Wu, Z. Wang, M. Yuan, J. Miao, Z. Lv, L. Xu, B. Wei, Mater. Today Energy 23 (2022) 100887.
[56] K. Chang, D.T. Tran, J. Wang, K. Dong, S. Prabhakaran, D.H. Kim, N.H. Kim, J.H. Lee, Appl. Catal. B Environ. 338 (2023) 123016.
[57] J. Jiang, M. Tong, D. Shen, Z. Liang, Z. Li, G. Duan, L. Wang, H. Fu, Adv. Funct. Mater. (2025). https://doi.org/10.1002/adfm.202500065.
[58] S. Guan, B. Xu, X. Yu, Y. Ye, Y. Liu, T. Guan, Y. Yang, J. Gao, K. Li, J. Wang, ACS Catal. 14 (2024) 17806–17817.
[59] L. Sun, M. Feng, Y. Peng, X. Zhao, Y. Shao, X. Yue, S. Huang, J. Mater. Chem. A 12 (2024) 8796–8804.
[60] M.J. Craig, G. Coulter, E. Dolan, J. Soriano-López, E. Mates-Torres, W. Schmitt, M. García-Melchor, Nat. Commun. 10 (2019) 4993.